Nanoscale

Accepted Manuscript

This article can be cited before page numbers have been issued, to do this please use: Y. Shu, W. Zhang, H. Cai, Y. Yang, X. Yu and Q. Gao, *Nanoscale*, 2019, DOI: 10.1039/C9NR00333A.

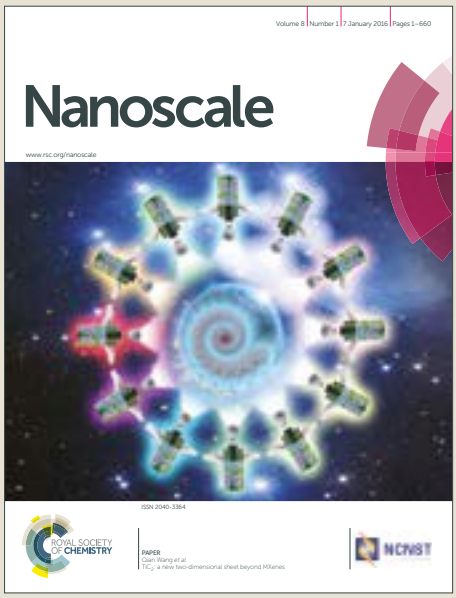

ROYAL SOCIETY OF CHEMISTRY

rsc.li/nanoscale

ROYAL SOCIETY OF CHEMISTRY View Article Online
DOI: 10.1039/C9NR00333A

Journal Name

ARTICLE

Expanding Interlayers of Molybdenum Disulfide toward Highly Sensitive Sensing of Hydrogen Peroxide

Received 00th January 20xx,
Accepted 00th January 20xx

DOI: 10.1039/x0xx00000x

www.rsc.org/

Yijin Shu,[a] Wenbiao Zhang,[a] Huaihong Cai,[a] Yang Yang,[a] Xiang Yu[ab] and Qingsheng Gao*[a]

ABSTRACT: Expandable interlayers in two-dimensional (2D) transition metal dichalcogenides enable the regulation on physicochemical properties toward boosted applications. Herein, interlayer-expanded MoS_2 (IE-MoS_2) are designed as sensitive electrochemical biosensors for H_2O_2, via a one-step hydrothermal process employing excessive thiourea. This facile fabricaion sucessfully avoids the complicated manipulations in conventional exfoliation-ressembling strategies. The as-obtained IE-MoS_2 features its expanded interlayer-spacing of 9.40 Å and the metallic electronic configurations. Thereby, it gains the good conductivity and more importantly the enhanced binding with *OH intermediate, accomplishing the fast kinetics of H_2O_2 reduction ($H_2O_2+2e^-\rightarrow 2OH^-$) and consequently the sensitive response in electrochemical H_2O_2 sensing. The optimal IE-MoS_2 affords a high sensitivity (1706.0 μA mM^{-1} cm^{-2}) and a low detection limit (0.2 μM), outperforming non-expanded MoS_2 (738.0 μA mM^{-1} cm^{-2}, 1.0 μM) and most of previsouly reported materials free from enzymes. Moreover, it performs well in real samples and under various interfering, and can be used to measure the intracellular H_2O_2 amount of cancer cells, predicting the promise in real-time monitoring, clinical diagnosis and pathophysiology. This work will inspire the rational design of 2D sensing materials via regulating their interlayer chemistry.

Introduction

Two-dimensional (2D) transition metal dichalcogenides (TMDs) have been extensively investigated in the field of energy storage/conversion,[1,2] catalysis,[3] sensing,[4,5] etc., owing to their unique optical/electronic properties and versatile chemistry. As a representative TMDs, molybdenum disulfide (MoS_2) adopts a layered crystal integrating atomic S-Mo-S slabs via weak van der Waals forces.[6] The resulting expandable interlayers serve as the key to boost physicochemical properties and accordingly applications.[7,8] For example, the engineering on MoS_2 to an expanded structure can decrease the diffusion energy barriers for guest ions in interlayers,[9] and optimize the electronic configurations on surface,[8] leading to high performance in reversible metal-ion (Li^+, Na^+ and Mg^{2+}) batteries[9-11] and electrocatalytic water splitting.[12] And, controlled cation (e.g., Li^+, Na^+ and K^+) intercalation allows for large photoluminescence modulation toward efficient sensing in biological systems.[13-15]

MoS_2-based nanostructures are functional segments of biosensing platforms to detect proteins,[16,17] DNA,[18-20] cancer cells,[21] cellular metabolism products,[22,23] etc. In particular, the detection of hydrogen peroxide (H_2O_2) attracts much attention.[24] H_2O_2 not only plays a key role in cell proliferation and death, response to chronic diseases, and intracellular signaling transduction, but also is one of the most stable species and a typical representative of reactive oxygen species in living organisms.[25-27] There is a strict demand for high sensitivity and low detection limit due to the trace H_2O_2 produced in living systems.[28,29] However, conventional MoS_2 cannot meet the demands because of the low sensitivity on undefined surface. Although uploading active enzymes or noble metals onto MoS_2 can improve sensitivity,[30,31] the research unfortunately loses sight of the physicochemical merits of MoS_2, and will cause poor stability and high cost. Regarding the sensing as a feedback of electrocatalytic H_2O_2 reduction ($H_2O_2+2e^-\rightarrow 2OH^-$),[32] the rational engineering on active surface is the key to address the dynamic energy barriers of reduction during sensing. Interlayer-expanded MoS_2 (IE-MoS_2) that features the regulated interlayers and electronic configurations, is anticipated to afford good sensitivity, definition and resolution for H_2O_2 detection,[33] even free from enzymes and noble-metal nanoparticles.

Herein, a facile hydrothermal process employing excessive thiourea (molar S/Mo = 12.0) is introduced to fabricate IE-MoS_2 nanoflowers with an expanded interlayer-spacing of 9.40 Å, *vs*. 6.15 Å in 2H phase MoS_2 (2H-MoS_2), leading to superior

[a] College of Chemistry and Materials Science, Jinan University, Guangzhou 510632, China. E-mail: tqsgao@jnu.edu.cn
[b] Analytic and Testing Centre, Jinan University, Guangzhou 510632, China
† Footnotes relating to the title and/or authors should appear here.
Electronic Supplementary Information (ESI) available: Elemental analysis, TGA and EDS of IE-MoS_2, TGA, FT-IR and XPS of samples derived from IE-MoS_2 after treatment, and the corresponding sensing performance. See DOI: 10.1039/x0xx00000x

performance for H_2O_2 sensing. The IE-MoS_2 is achieved at short reaction time owing to the strong interactions between thiourea and MoS_2 monolayers, and it degrades to a thermodynamically preferred but unexpanded 2H phase in prolonged reaction after thiourea decomposition. As evidenced by experimental and theoretical investigations, the IE-MoS_2 features its metallic electronic configuration around the Fermi level (E_F), which promotes the conductivity and more importantly enhances the binding with *OH intermediate. Thereby, the promoted H_2O_2 reduction results in a highly sensitive response. It affords a high sensitivity (1706.0 μA mM^{-1} cm^{-2}) and a low detection limit (0.2 μM) for H_2O_2 sensing, superior to non-expanded MoS_2 (NE-MoS_2, 738.0 μA mM^{-1} cm^{-2}, 1.0 μM) and even most of materials free from enzymes and noble-metals. Moreover, the IE-MoS_2 shows outstanding selectivity to H_2O_2 under various interfering by ascorbic acid (AA), glucose, sucrose, uric acid (UA), dopamine (DA), NaCl and KCl, and performs well in real samples (e.g., serum, juice and milk). It can be further used to detect the intracellular H_2O_2 amount of human breast cancer cells (MCF-7), highlighting the promise in real-time monitoring, clinical diagnosis and pathophysiology.

Results and discussion

A hydrothermal process is introduced to prepare IE-MoS_2 in a shape of nanoflowers, in which excessvie thiourea (molar S/Mo = 12.0) and short reaction time (e.g., 3.0 h) are adopted (Fig. 1a). The prolonged reaction leads to NE-MoS_2 with a thermodynamically preferred 2H phase. As shown in scanning electronic microscopy (SEM) images (Fig. 1a), sphere-like products in micron size are initially received (e.g., at 1.0 h), which are precursors to generate nanosheets afterwards, and finally degrade to smaller nanoflowers after 3.0 h. X-ray diffraction (XRD) investigation presents according evolution in crystallographic structure (Fig. 1b). The samples received at 1.0 ~ 3.0 h show the consistent patterns with characteristic diffraction peaks at 2ϑ = 9.3°, 18.6°, 33.2°, and 57.4°, which can be indexed as the (002), (004), (100) and (110) of the IE-MoS_2, respectively. The (002) and (004) correspond to the obviously larger d-spacing of 9.40 and 4.70 Å, in comparison with those of 2H-MoS_2 (6.15 and 3.08 Å), but the (100) and (110) experience negligible variation. This observation indicates the expanded lattice along the c axis, but negligible in the ab plane (Inset of Fig. 1b). Accordingly, the simulated pattern of such an interlayer expanded structure fits well with the experimental results. After a prolonged reaction for 6.0 h, the characteristic peak of 2H-MoS_2(002) emerges at 2ϑ = 14.3°, associated with the partial degradation of IE-MoS_2 to NE-MoS_2. Such phase evolution will be completed after 12.0 h, as indicated by the disappearance of the IE-MoS_2 pattern. For convenience, the samples received at different time (t = 1.0 ~ 6.0 h) are denoted as IE-MoS_2(*t*), and that received at 12.0 h,

View Article Online DOI: 10.1039/C9NR00337A

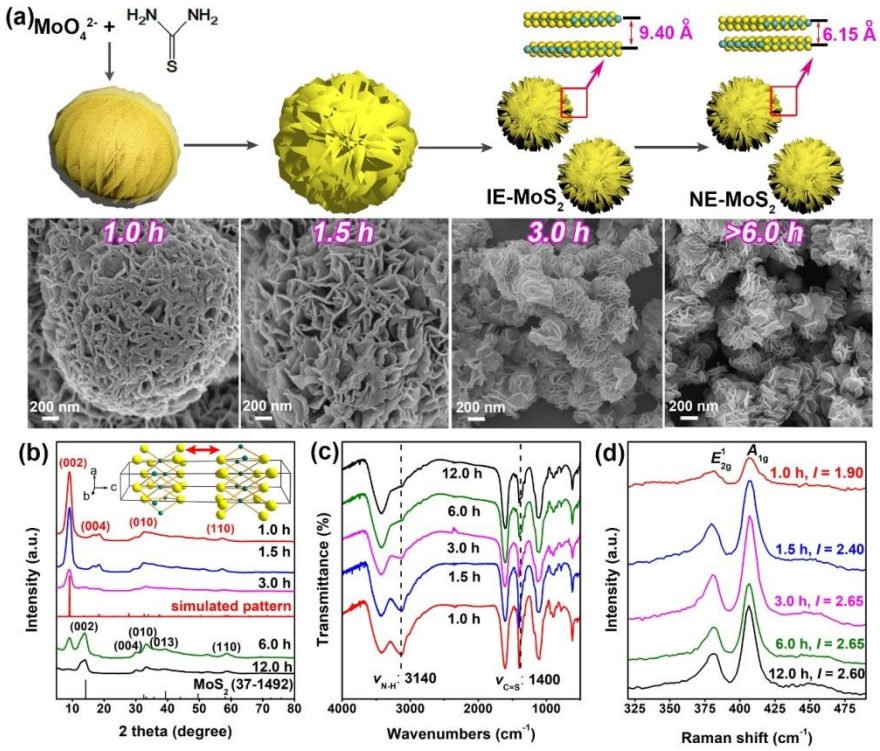

Fig. 1 (a) Schematic illustration for IE-MoS_2 preparation and the corresponding SEM images. (b) XRD patterns, (c) FT-IR spectra and (d) Raman spectra of samples obtained at different reaction time.

View Article Online
DOI: 10.1039/C9NR00333A

with non-expanded interlayers, is accordingly assigned to NE-MoS_2.

that the rich edges on MoS_2 are well-retained even after shrinking interlayers.

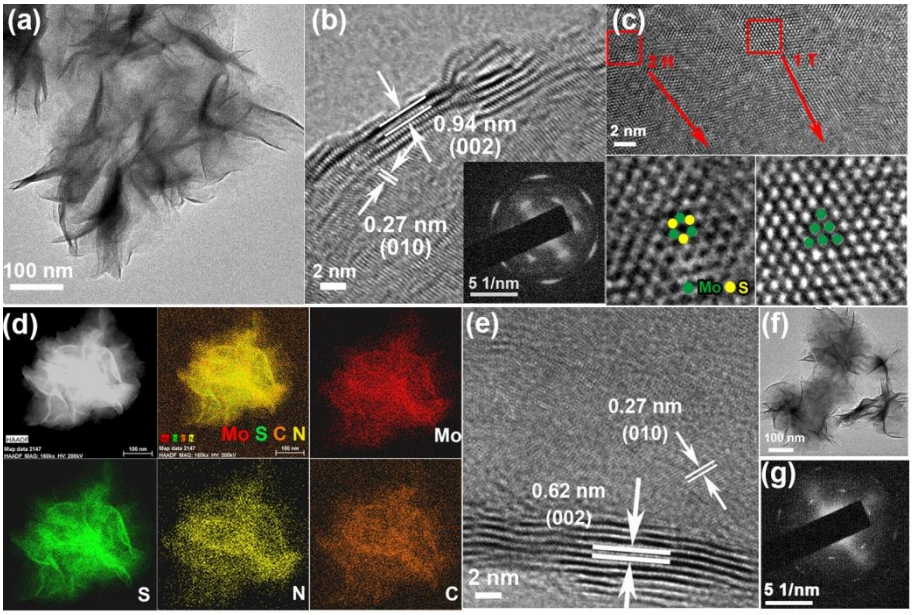

Fig. 2 (a) TEM, (b) HR-TEM, and (c) AC-TEM images of the IE-MoS_2(*3.0*), and (d) HAADF-STEM images along with the corresponding elemental mapping. Inset of (b) is the SAED pattern obtained on the nanosheet. (e and f) TEM images and (g) SAED pattern of the NE-MoS_2 obtained after reaction for 12.0 h.

Fourier-transform infrared (FT-IR) spectroscopy, thermogravimetric analysis (TGA) and Raman spectroscopy are further taken to analyze the structural evolution. As shown in FT-IR (Fig. 1c), the bands associated with the stretching vibrations of N-H (3140 cm^{-1}) and C-S (1400 cm^{-1}) bonds gradually become weak as the reaction is prolonged, indicating the decomposition of thiourea in samples. The elemental analysis gives a direct proof for the decreasing C and N contents (Table S1†). Accordingly, the TGA profiles present a weight loss at 180 ~ 350 °C from the IE-MoS_2 due to thiourea decomposition (Fig. S1†). By contrast, the weight loss in the NE-MoS_2 is relatively slight. Regarding the clear correlation between structural evolution (from IE-MoS_2 to NE-MoS_2) and thiourea decomposition, the interlayer expanding is reasonably ascribed to the intercalation of excessive thiourea into MoS_2 lattice. As thiourea is not largely excessive (e.g., S/Mo = 3.0 and 6.0), only the NE-MoS_2 is obtained (Fig. S2†), confirming interlayer expanding due to excessive thiourea intercalation. Meanwhile, Raman investigation presents two peaks at 380.9 and 406.8 cm^{-1} (Fig. 1d), corresponding to the in-plane (E_{2g}^1) and out-of-plane (A_{1g}) modes of Mo-S in MoS_2 interlayers,[12] respectively. The ratio (I) of A_{1g}/E_{2g}^1 can be used to identify the surface textures, and the high value suggests the large proportion of edge-terminated structure.[34] Observably, such value increases with reaction time from 1.0 to 3.0 h, because of the enriched edges on the IE-MoS_2. However, it keeps at a consistent level of 2.60 ~ 2.65 in the IE-MoS_2(*3.0*), IE-MoS_2(*6.0*) and NE-MoS_2, different from the visible evolution in crystallographic structure. It's indicated

Transition electronic microscopy (TEM) shows more details for the expanded interlayers of the IE-MoS_2. As displayed in Fig. 2a, the IE-MoS_2(*3.0*) nanoflowers consist of thin nanosheets. The closer observation confirms an interlayer d-spacing of 0.94 nm (Fig. 2b) on the curled-up edges, corresponding to the expanded (002) facet identified by XRD (*c.f.* Fig. 1b). A lattice fringe of 0.27 nm observed on nanosheets is ascribed to the (010) or (100). Noticeably, the selected area electronic diffraction (SAED) pattern with dispersive plots suggests rich defects on the nanosheets (inset of Fig. 3b), which may be a result of thiourea intercalation. Furthermore, aberration-corrected TEM (AC-TEM) clearly identifies both trigonal prismatic 2H and octahedral 1T phases in the IE-MoS_2 nanosheets (Fig. 2c). The weakened interactions between two adjacent MoS_2 monolayers in the IE-MoS_2(*3.0*) will drive the partial phase transformation from 2H to 1T.[35] Moreover, the energy dispersive spectroscopy (EDS) attached on TEM confirms the presence of Mo, S, C and N in the IE-MoS_2(*3.0*) (Fig. S3†), and the corresponding elemental mapping shows their uniform distribution (Fig. 2d). By contrast, the NE-MoS_2 received after a prolonged reaction (12.0 h) presents a shrinking interlayer spacing of only 0.62 nm (Fig. 2e and 2f), associated with the characteristic (002) of 2H-MoS_2. The observable interlayer shrinkage, in good line with XRD, is owing to thiourea decomposition. Afterward, the crystallinity of nanosheets increases, as suggested by the relatively sharp SAED pattern (Fig. 2g) in comparison with that of the IE-MoS_2(*3.0*).

View Article Online
DOI: 10.1039/C9NR00333A

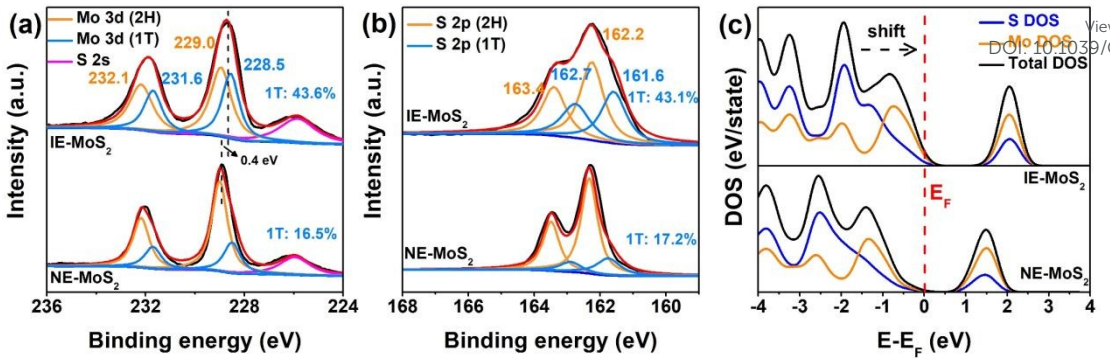

Fig. 3 XPS spectra of (a) Mo 3d and (b) S 2p in the IE-MoS_2(*3.0*) and NE-MoS_2. (c) DOS for the IE-MoS_2 and NE-MoS_2.

The electronic configurations on the IE-MoS_2 will be altered because the coupling of electronic orbitals is relaxed within expanded interlayers. X-ray photoelectron spectroscopy (XPS) is employed to investigate the different chemical states in the IE-MoS_2 and NE-MoS_2. In the Mo 3d profiles (Fig. 3a), the peaks at 228.5 ~ 229.0 eV and 231.6 ~ 232.1 eV are ascribed to the Mo $3d_{5/2}$ and $3d_{3/2}$ of Mo^{4+} in MoS_2, and that at 226.3 eV corresponds to the S 2s.[36,37] Observably, the IE-MoS_2(*3.0*) exhibits a red-shift for Mo 3d in comparison with the NE-MoS_2, indicating enriched electrons around Mo sites after interlayer expanding. The further deconvolution of these peaks reveals two doublets. The one at 229.0 and 232.1 eV corresponds to Mo^{4+} in 2H-MoS_2, and the other shifting to lower binding energies by ~0.5 eV (i.e., 228.5 and 231.6 eV) can be ascribed to 1T-MoS_2.[38] Noticeably, the IE-MoS_2(*3.0*) shows more 1T phase than the NE-MoS_2, according to the higher content of 43.6% than that of the latter (16.5%). Meanwhile, the XPS profiles of S 2p afford the consistent variation, and more S species from 1T-MoS_2 is observed on the IE-MoS_2(*3.0*) (Fig. 3b). To have an insight into the varied electronic configuration, we then performed DFT calculation on the IE-MoS_2 and NE-MoS_2. Fig. 2c shows that the density of states (DOS) of the IE-MoS_2 is shifted upwards as compared with the NE-MoS_2. As a result, there are enriched states going across the E_F, indicating the metallic electronic configuration that would facilitate electron excitation/ transfer.[8] This result is consistent with the previous report on MoS_2 intercalated by N,N-dimethylformamide species.[12] In further respect to elemental orbitals, both Mo and S move up toward the E_F, which can be used to interpret the red-shifted binding energy in XPS profiles.

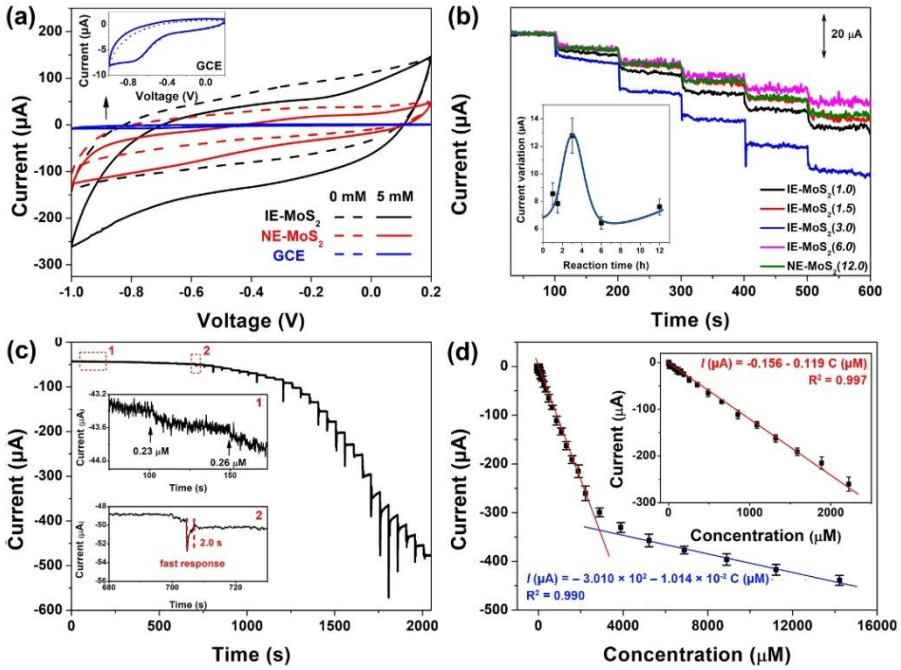

Fig. 4 (a) Amperometric i-t curves of various IE-MoS_2 modified GCEs in a N_2-saturated PBS (0.01 M) solution responding to a successive addition of 100 μM H_2O_2, and (b) the corresponding average variation in currents. (c) Amperometric response of a IE-MoS_2(*3.0*) modified GCE to dropwise adding H_2O_2, and (d) calibration curve of current versus H_2O_2 concentration.

Table 1. Comparison of electrochemical H_2O_2 sensors reported previously with the IE-MoS_2(3.0).

material	sensitivity ($\mu A\ mM^{-1}\ cm^{-2}$)	linear range (μM)	LOD (μM)
IE-MoS_2(*3.0*)	1706.0/144.9	0.23-2200/ 2200-14220	0.2
NE-MoS_2	738.0/67.1	2.3-2200/ 2200-14200	1.0
HRP-MoS_2-Gr[30]	679.7	0.2-1103	0.049
Catalase/MoS_2-Au/chitosan[39]	187.4	0.5-200	0.1
MoS_2-Au/Pt[31]	142.68	10-19070	0.39
Au-Pd/MoS_2[40]	184.9	0.8-10000	0.16
Ag-Fe_2O_3-rGO[41]	50.8	1.6-57000	0.5
Ag/ZSM-5[42]	71	30-14000	2.5
Ag@MOF/GO[43]	80.23	4-11000	0.18
NG/Ag NPs[44]	/	5-47000	0.56
rGO-Pt[45]	459	0.5-3470	0.2
Pt/rGO[46]	132.8	5-3000	0.4
Pd nanocubes[47]	287.7	100-24000	7.5
Cu_2O-rGO[48]	295	30-12800	21.7
MWCNT/MnO_2[49]	219.05	5-4530	0.952
ZnO/Co_3O_4/$NiCo_2O_4$[50]	388	0.2-2400	0.163
O_x-CNTs@CeO_2[51]	160	100-1400	2.7

In electrochemical H_2O_2 sensing, the IE-MoS_2 and NE-MoS_2 are modified onto glassy carbon electrodes (GCEs) to measure the electrochemical signals responding to H_2O_2 injection (Fig. 4a). A bare GCE delivers negligible current response to 5 mM H_2O_2 in cyclic voltammograms (CVs), guaranteeing a minimal background. In sharp contrast, the IE-MoS_2(*3.0*) modified GCE affords an obviously increasing current due to the promoted H_2O_2 reduction to OH^-, and performs more sensitively than the NE-MoS_2. The more details for H_2O_2 detection are further analyzed by amperometric i-t curves in response to H_2O_2 concentration (Fig. 4b). The test is conducted by successively adding H_2O_2 into a phosphate buffer saline (PBS, 0.01 M) solution, at a working potential of -0.65 V *vs.* Ag/AgCl (3 M KCl). The IE-MoS_2(*3.0*) exhibits a maximum increase in current (inset of Fig. 4b). In comparison, the IE-MoS_2(*6.0*) and NE-MoS_2 (received after 12 h) give the less increase, along with the phase evolution from IE-MoS_2 to NE-MoS_2. It's suggested that the high sensitivity is correlated with the expanded structure of IE-MoS_2. Although the IE-MoS_2(*1.0*) and IE-MoS_2(*1.5*) samples possess similar expanded interlayers, the bulky dimension in micron cannot fully expose active edge-sites (*c.f.* Raman data in Fig. 1d), thereby affording lower response. In addition, the IE-MoS_2(*3.0*) is also sensitive to H_2O_2 at other potentials (e.g., -0.45 and -0.20 V), as shown in Fig. S4†.

Fig. 4c further presents its typical current-time plot responding to stepwise H_2O_2 injection into N_2-saturated 0.01 M PBS. It affords a visible response to a low H_2O_2 concentration of only 0.23 μM, and the response is quick (~ 2.0 s) and stable (insets of Fig. 4c). Accordingly, Fig. 4d displays the linear plots of current *vs.* H_2O_2 concentration in a range of 2.3 × 10^{-1} to 14. 2 × 10^3 μM. There are two linear calibration plots corresponding to the low (2.3 × 10^{-1} ~ 2.2 × 10^3 μM) and medium (4.0 × 10^3~ 14.2 × 10^3 μM) concentration ranges. They fit well regression equations of *I* (μA) = –0.156 – 0.119 × C (μM) (R^2 = 0.997) and *I* (μA) = – 3.010 × 10^2 – 1.014 × 10^{-1} × C (μM) (R^2 = 0.990), respectively. Remarkably, the sensitivity in the low concentration range is as high as 1706.0 $\mu A\ mM^{-1}\ cm^{-2}$, and the limit of detection (LOD) is 0.2 μM (LOD = 3 × relative standard deviation/slope[52]). These merits are superior to those on the NE-MoS_2 (sensitivity: 738.0 $\mu A\ mM^{-1}\ cm^{-2}$, LOD: 1.0 μM, Fig. S5†), IE-MoS_2(*1.0*) and IE-MoS_2(*1.5*) (Fig. S6 and S7†). It highlights a promise to meet the strict requirement for H_2O_2 detection in biomedical diagnosis. In further comparison with the recently reported materials, the IE-MoS_2(*3.0*) performs at a high level (Table 1). Its sensitivity or LOD outperforms those involving enzymes, precious metals, or metal oxides, e.g., catalase/MoS_2–Au/chitosan,[39] MoS_2-Au/Pt,[31] Ag-Fe_2O_3-rGO,[41] and O_x-CNTs@CeO_2,[51] etc.

To confirm the promotion associated with expanded interlayers, we degrade the IE-MoS_2(*3.0*) and then test the sensing performance. Three post treatments of (i) calcination under an Ar flow, (ii) hydrothermal treatment by 0.01 M H_2SO_4, and (iii) Ar-plasma clean were adopted, and the products denoted as MoS_2-C, MoS_2-H, and MoS_2-AP were received, respectively. As shown in XRD (Fig. 5a), the MoS_2-C and MoS_2-H clearly identify the degradation to 2H-MoS_2, because the calculation (350 °C, Ar) and hydrothermal (0.05 M H_2SO_4, 150 °C) treatments can decompose the intercalating thiourea.[37] By contrast, a mild Ar plasma treatment in short time (90 seconds) and with a low power (20 W) only leads to the partially shrinked interlayers in MoS_2-AP, as indicated by the wide peak at 2ϑ = 7.5 ~ 15.0°. Such alteration is accordingly confirmed by the TGA and FT-IR analysis (Fig. S8†).

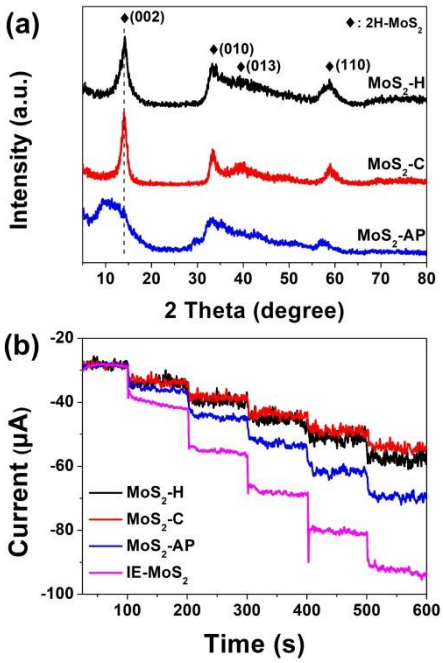

Fig. 5 (a) XRD patterns of samples derived from the IE-MoS_2 via different post treatments, and (b) their amperometric i-t curves in a N_2-saturated PBS (0.01 M) solution responding to a successive addition of 100 μM H_2O_2.

View Article Online
DOI: 10.1039/C9NR00333A

The above samples are further subjected to sensing H_2O_2 (Fig. 5b). The MoS_2-C and MoS_2-H without expanded interlayers deliver obviously decreased currents responding to H_2O_2 injection, in comparison with the IE-MoS_2(*3.0*). With the partially retained IE structure, the MoS_2-AP only suffers a mild decrease in responding currents. Given that the above samples remain the consistent edge-terminated structures (*c.f.* Raman in Fig. S9†), the different sensing behavior confirms the key promotion on expanded MoS_2 interlayers. The XPS (Fig. S10†) proves the altered binding energy of both Mo and S due to interlayer shrinkage (e.g., IE-MoS_2 *vs*. MoS_2-H), highlighting the correlation between sensitivity and electronic configurations on expanded MoS_2. Such correlation is further supported by IE-MoS_2 fabricated with thioacetamide (Fig. S11†), in which the IE-MoS_2 always delivers more sensitive response than that of the NE-MoS_2, despite the different intercalating molecules.

According to previous reports,[25,53] the reduction of H_2O_2 proceeding via a OH intermediate bonded on material surface (denoted as *OH) is accounting for the electrochemical response in H_2O_2 sensing (Fig. 6a). The binding of *OH is the key factor, and the stronger one will promote the cleavage of O-O bond in a dissociation process that is considered as the rate-determining step of H_2O_2 reduction. In this regard, DFT calculation is employed to uncover the different binding energy of *OH on the IE-MoS_2 and NE-MoS_2. As proved previously,[54] the *OH is preferably bonded with the edge sites of MoS_2, rather than the basal (002) facet. Thereby, the Mo and S terminated edge sites, i.e., MoS_2 (100) and (010), respectively, are taken into account. The calculation shows that *OH binding on (100) is thermodynamically favored on both IE-MoS_2 and NE-MoS_2, in comparison with (010) (Fig. S12†). Fig. 6b presents the chemisorption of *OH and the binding energy on the (100). The value on the IE-MoS_2 is -3.13 eV, lower that on the NE-MoS_2 (-2.95 eV), which indicates the stronger chemisorption on the former. Moreover, the OH^- affinity was further evaluated through the oxidative scans in N_2-saturasted 0.5 M NaOH.[55] As shown in Fig. 6c, the potential for surface OH^- adsorption on the IE-MoS_2(*3.0*) is more negative than that on the NE-MoS_2, suggesting OH^- is easier to achieve adsorption equilibrium on the former due to the strong *OH binding. This strong *OH binding on edge sites can promote the kinetics of H_2O_2 reduction ($H_2O_2+2e^-\rightarrow 2OH^-$), and consequently the sensing response. In addition, the metallic band states and the consequently improved conductivity of IE-MoS_2 also facilitate the charge transfer during H_2O_2 reduction. Thereby, the IE-MoS_2 accomplishes the prominent performance for H_2O_2 sensing.

The selectivity of the IE-MoS_2(*3.0*) is practically and extremely important for H_2O_2 detection. During H_2O_2 sensing, ions and small molecule compounds (e.g., AA, glucose, sucrose, UA, DA, NaCl and KCl) presenting in body fluids are interfering substances.[39] After injecting the above substances (100 μM), the amperometric response exhibits negligible change (Fig. 7a), demonstrating the high selectivity of H_2O_2 on the IE-MoS_2. Another important focus is the long-time stability of sensor. Fig. 7b shows the satisfactory stability after injecting 100 μM H_2O_2, keeping a stable current during ~ 3000 s.

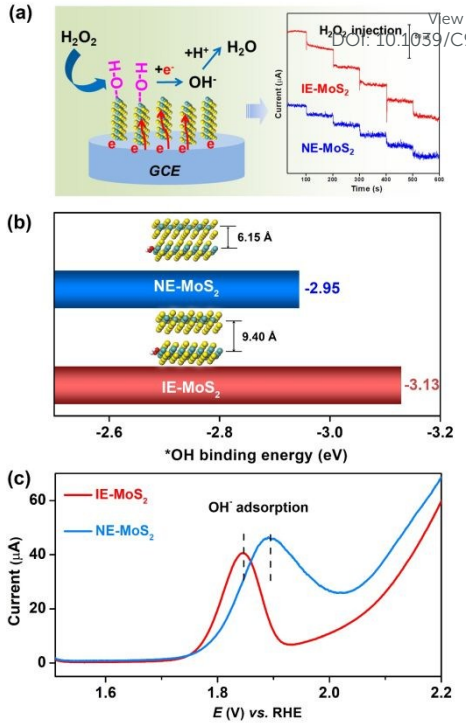

Fig. 6 (a) Schematic illustration for H_2O_2 sensing on MoS_2 modified GCEs. (b) Chemisorption configuration and corresponding binding energy of *OH on the (100) facet of the IE-MoS_2 and NE-MoS_2. (c) Single oxidative linear scans for the IE-MoS_2(*3.0*) and NE-MoS_2 in N_2-saturasted 0.5 M NaOH.

To verify the feasibility of the proposed sensor for H_2O_2 detection in real samples, H_2O_2 in grape juice, apple juice, milk and serum was analyzed by the IE-MoS_2(*3.0*) modified GCEs. The above samples represent practical significance, because H_2O_2 as an additive is often used in production and storage processes in beverage and milk industry,[56] and H_2O_2 concentration in body fluids is linked with many cell functions. Fig. 7c displays the amperometric response to H_2O_2 injection in presence of grape juice, apple juice, milk and serum, which shows the well-retained sensitivity at a high level. The recoveries are as high as 90.6-96.0% in milk, 93.7-102.2% in apple juice, 101.1-107.9% in grape juice, and 97.1-109.7% in serum. The efficiency of the IE-MoS_2 sensing platform is highlighted in various environments.

Because intracellular H_2O_2 is an important signaling molecule for the regulation of many biological processes,[57] we further use the IE-MoS_2(*3.0*) to detect H_2O_2 level in living cancer cells, e.g., human breast cancer cells (MCF-7). External Phorbol 12-myristate 13-acetate (PMA) was used as stimulator to release H_2O_2 because PMA could disrupt intracellular redox homeostasis of cancer cells and then produce H_2O_2.[58] As shown in Fig. 7d, after injecting PMA, the current obviously increases in presence of MCF-7 cells, and it gradually returns to a background level when catalase is subsequently added to decompose H_2O_2. By contrast, the current response without MCF-7 is quite negligible. This identifies that the current

View Article Online
DOI: 10.1039/C9NR00333A

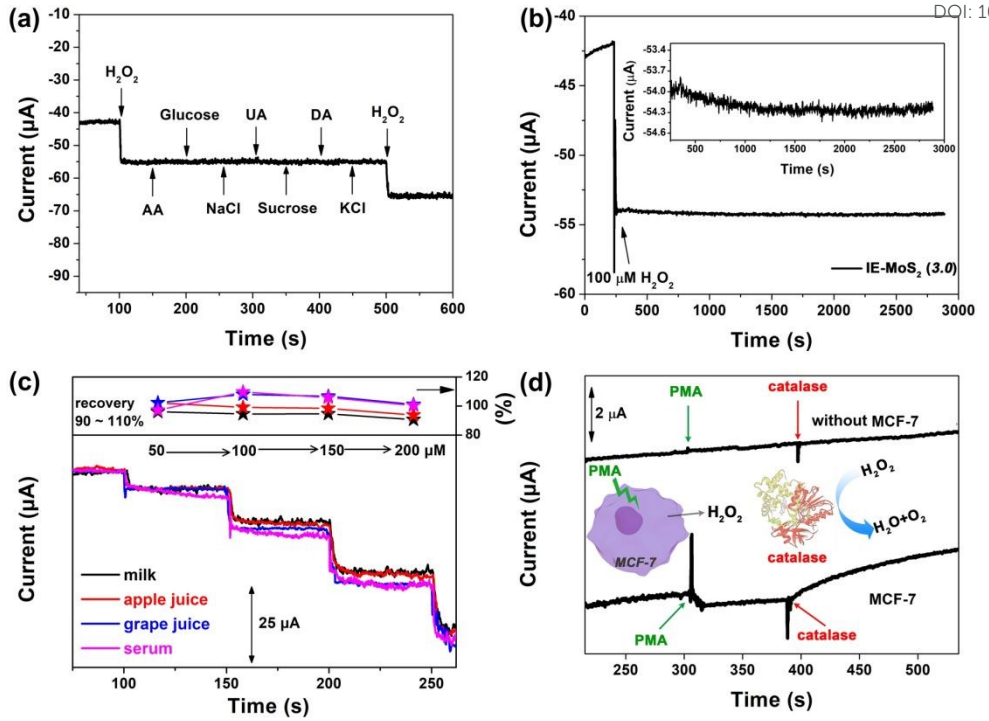

Fig. 7 (a) Amperometric i-t curves on GCEs modified by the IE-MoS_2(*3.0*) in a N_2-saturated PBS (0.01 M) solution responding to 100 μM H_2O_2 in presence of various interfering substances (100 μM). (b) Current response to injecting 100 μM H_2O_2 during a long period time (~ 3000 s). (c) i-t curves on IE-MoS_2(*3.0*) modified GCEs for H_2O_2 detection in milk, apple juice, grape juice and serum. (d) Current response on IE-MoS_2(*3.0*) modified GCEs to introducing PMA and catalase into 0.01 M PBS with or without MCF-7 cells (cell concentration: 1×10^5 cells mL^{-1}).

increase is owing to H_2O_2 released from MCF-7. The variation of current is 0.45 μA, corresponding to 3.8 μM H_2O_2 released from MCF-7 cells. And the amount of H_2O_2 produced by per cell is estimated to be 3.8×10^{-8} μmol $cell^{-1}$, agreeing well with the reported value for MCF-7 cells.[59] These results demonstrate the capability of IE-MoS_2 to determine extracellular H_2O_2, as well as the promise in clinical diagnose.

Conclusions

Interlayer expanded MoS_2 (9.40 Å) nanoflowers are controllably fabricated via a facile hydrothermal process employing excessive thiourea, which accomplish superior sensitivity in electrochemical H_2O_2 detection. The strong interactions between thiourea and MoS_2 monolayers are beneficial for the formation of such kinetically favored phases with expanded interlayers. The optimal IE-MoS_2 affords the high sensitivity (1706 μA mM^{-1} cm^{-2}) and low detection limit (0.2 μM), which stem from the interlayer expanded structures. The metallic electronic configuration around the E_F can lead to the enhanced binding with *OH intermediates and the promoted conductivity, which are vital in electrochemical H_2O_2 detection. Moreover, the designed IE-MoS_2 performs well in real samples and under various interfering, and can be used to measure the intracellular H_2O_2 amount of cancer cells. It is envisioned that the systematic engineering on interlayer spacing by varied thiols, or covalence functionalization of monolayer surface,[60,61] will further boost the sensing performance of 2D materials.

Experimental

Materials and IE-MoS_2 synthesis

Ammonium heptamolybdate tetrahydrate ($(NH_4)_6Mo_7O_{24}\cdot4H_2O$, AHM), thiourea, hydrogen peroxide and PBS were purchased from Sinopharm Chemical Reagent Co. Ltd (Shanghai, China). PMA, catalase and nafion solution (5 wt% in lower aliphatic alcohols and water) were purchased from Sigma-Aldrich. All chemicals were of analytical grade and used as received without further purification. All aqueous solutions were prepared using ultrapure water (>18 MΩ).

A hydrothermal process employing excessive thiourea was adopted. Typically, 0.353 g of AHM and 1.830 g of thiourea (molar S/Mo = 12.0) were dissolved in 15 mL of distilled water, and then was stirred for 30 minutes to get a clean solution. The solution was transferred to a Teflon-lined stainless steel autoclave, and heated at 240 °C for 3 h. The solid was collected by centrifugation, thoroughly washed with water and ethanol, and then dried at 50 °C overnight. The IE-MoS_2 with

visibly expanded interlayers was thereby fabricated. As the hydrothermal reaction was prolonged to 12 h, the NE-MoS_2 was received.

To degrade the expanded interlayers in the IE-MoS_2, there post-treatments were conducted. (i) Calcination. The IE-MoS_2(*3.0*) was heated at 350 °C for 2 h under an argon flow (100 mL min^{-1}). (ii) Hydrothermal treatment by H_2SO_4. 0.1 g of IE-MoS_2(*3.0*) was dispersed into 15 mL of diluted H_2SO_4 (0.05 mol L^{-1}), and treated at 150 °C for 2 h. (iii) Ar-plasma clean. The IE-MoS_2(*3.0*) was placed in a tubular oven equipped with a plasma generator and treated in Ar for 90 seconds with a small RF power of 20 W. The received samples were denoted as MoS_2-C, MoS_2-H and MoS_2-AP, respectively. The former two can degrade the IE-MoS_2 to typical 2H-MoS_2, because of the complete removal of thiourea in such harsh treatment. By contrast, the Ar-plasma treatment results in the partial degradation of the expanded interlayers.

Physical characterization

SEM was taken on a ZEISS ULTRA55. TEM, EDS, HAADF-STEM and elemental mapping were taken on a JEOL JEM 2100F. AC-TEM was collected on a JEOL JEM-ARM 200F. XRD investigation was performed on Bruker D8 Advance diffractometer with Cu Kα radiation (λ = 1.54056 Å). The N, C and S contents in samples were determined by CHNS elemental analysis on a Vario EL Elementar. FT-IR spectra were collected on a Nicolet 6700 FTIR spectrometer. Raman spectra were recorded on a laser confocal Raman microspectrometer (HR-800, Horiba Jobin Yvon, Ltd.), with an excitation laser wavelength of 532 nm. XPS was processed on a Thermo scientific (Escalab 250Xi), using C 1s (284.6 eV) as a reference. TGA was performed on a NETZSCH STA449F3 under N_2 flow with a heating rate of 5 °C min^{-1}.

Electrochemical measurement

4 mg of MoS_2-based materials and 40 μL of 5 wt% Nafion solution solution were dispersed in 1 mL water–ethanol with a $V_{water}/V_{ethanol}$ ratio of 4 : 1, and then the mixture was vigorously sonicated for at least 30 min to achieve a homogeneous ink. The as-obtained solution (5 μL) was loaded onto a GCE (3 mm diameter), and dried naturally in air. A conventional three-electrode system was employed on a CHI 650E electrochemical workstation (Chenhua Instruments Shanghai Co., Ltd, China). A Ag/AgCl (3 M KCl) electrode and a platinum wire were used as the reference and counter electrodes, respecticely. Electrochemical tests were carried out in 0.01 M PBS buffer.

To test the selectivity of the IE-MoS_2(*3.0*), 100 μM of interfering substances (AA, glucose, sucrose, UA, DA, NaCl and KCl) were injected into the solution during amperometric test. And pure milk (Mengniu Dairy), graphe juice (Huiyuan, 100%), apple juice (Huiyuan, 100%) and serum provided by volunteers are used as real samples to test the recovery. The above samples (grape juice: 300 μL, apple juice: 300 μL, milk: 30 μL, and serum: 30 μL) were at first dispersed into 30 mL of 0.01 M PBS. And then, H_2O_2 with varied concentrations were injected and the current responses were recorded at -0.65 V. All experiments were performed in accordance with the law prepared by the Institute of Laboratory Animal Resources, National Research Council, and published by the National Academy Press (1996), and approved by the ethics committee at Jinan University. Informed consents were obtained from human participants of this study.

Detection of intracelluar H_2O_2 released from MCF-7 cells

MCF-7 (human breast adenocarcinoma cell line) was obtained from Southern Medical University (Guangzhou, China). Cells were cultured in Dulbecco's Modified Eagle Medium (DMEM) supplemented with 10% fetal bovine serum, penicillin (100 U mL^{-1}), and streptomycin (100 μg mL^{-1}) in a humidified atmosphere at 37 °C in 5% carbon dioxide and 95% air. Cells were digested with 0.25 wt% trypsin at 37 °C for 120 s and separated from the culture medium by centrifugation (1000 rpm) for 5 min, and then washed with PBS (0.01 M, pH 7.4) for three times, and finally suspended in PBS to 1×10^6 cells mL^{-1}. The MCF-7 was mixed with 0.01 M PBS buffer to reach its concentration of 1×10^5 cells mL^{-1}. PMA was employed as the stimulant for intracellular H_2O_2 release. To detect H_2O_2 released from MCF-7, the amperometric current-time plot was performed on the IE-MoS_2 modified GCEs.

Theoretical Calculations

The OH adsorption energy (ΔE_{OH}) calculations on the edge of NE-MoS_2 and IE-MoS_2 were performed by Cambridge Sequential Total Energy Package (CASTEP) module in Material Studio. And ΔE_{OH} was calculated as:

$$\Delta E_{OH} = E_{(slab + adsorbate)} - E_{(slab)} - E_{(adsorbate)}$$

Where $E_{(slab + adsorbate)}$, $E_{(slab)}$ and $E_{(adsorbate)}$ were total energy of slab with adsorbate, the energy of pure slab/facet and the energy of adsorbate (OH) in the gas phase, respectively.

Generalized gradient approximation (GGA) with Perdew-Burke-Ernzerhof (PBE) functional was used for the exchange correlation energy. The kinetic energy cutoff for the plane-waves expansion was 400 eV. The self-consistent field (SCF) tolerance was 1×10^{-6} eV. The Brillouin zone was sampled by 3 × 3 × 1 k-points. 2H-MoS_2 and IE-MoS_2 crystal structure with an expanded interlayer spacing of 9.4 Å adopts a hexagonal crystal structure, using 2 × 2 × 1 supercell. Vacuum thickness of 12 Å was chosen to simulate the surface properties.

Conflicts of interest

There are no conflicts to declare.

Acknowledgements

We appreciate the financial support from National Natural Science Foundation of China (grant No.: 21773093 and 21433002), Guangdong Natural Science Funds for Distinguished Young Scholar (grant No.: 2015A030306014), and Guangzhou Science and Technology Program (grant No.:

201707010268). The authors greatly appreciate the supports from Prof. D. Li (Jinan University) in theoretical calculation.

Notes and references

1 M. Chhowalla, H. S. Shin, G. Eda, L.-J. Li, K. P. Loh and H. Zhang, *Nat. Chem.*, 2013, **5**, 263-275.
2 Q. Yun, Q. Lu, X. Zhang, C. Tan and H. Zhang, *Angew. Chem. Int. Ed.*, 2018, **57**, 626-646.
3 X. Zhang, Z. C. Lai, Q. L. Ma and H. Zhang, *Chem. Soc. Rev.*, 2018, **47**, 3301-3338.
4 X. Gan, H. Zhao and X. Quan, *Biosens. Bioelectron.*, 2017, **89**, 56-71.
5 C. Anichini, W. Czepa, D. Pakulski, A. Aliprandi, A. Ciesielski and P. Samori, *Chem. Soc. Rev.*, 2018, **47**, 4860-4908.
6 J.-O. Joswig, T. Lorenz, T. B. Wendumu, S. Gemming and G. Seifert, *Acc. Chem. Res.*, 2015, **48**, 48-55.
7 E. Benavente, M. A. Santa Ana, F. Mendizabal and G. Gonzalez, *Coordin. Chem. Rev.*, 2002, **224**, 87-109.
8 K. D. Rasamani, F. Alimohammadi and Y. Sun, *Mater. Today*, 2017, **20**, 83-91.
9 J. Xu, J. J. Zhang, W. J. Zhang and C. S. Lee, *Adv. Energy Mater.*, 2017, **7**, 1700571.
10 Z. Hu, L. X. Wang, K. Zhang, J. B. Wang, F. Y. Cheng, Z. L. Tao and J. Chen, *Angew. Chem. Int. Ed.*, 2014, **53**, 12794-12798.
11 Y. Liang, H. D. Yoo, Y. Li, J. Shuai, H. A. Calderon, F. C. R. Hernandez, L. C. Grabow and Y. Yao, *Nano Lett.*, 2015, **15**, 2194-2202.
12 M.-R. Gao, M. K. Y. Chan and Y. Sun, *Nat. Commun.*, 2015, **6**, 7493.
13 K. Kalantar-zadeh, J. Z. Ou, T. Daeneke, M. S. Strano, M. Pumera and S. L. Gras, *Adv. Funct. Mater.*, 2015, **25**, 5086-5099.
14 J. Z. Ou, A. F. Chrimes, Y. Wang, S.-y. Tang, M. S. Strano and K. Kalantar-zadeh, *Nano Lett.*, 2014, **14**, 857-863.
15 Y. Wang, J. Z. Ou, S. Balendhran, A. F. Chrimes, M. Mortazavi, D. D. Yao, M. R. Field, K. Latham, V. Bansal, J. R. Friend, S. Zhuiykov, N. V. Medhekar, M. S. Strano and K. Kalantar-zadeh, *ACS Nano*, 2013, **7**, 10083-10093.
16 X. Qiao, K. Li, J. Xu, N. Cheng, Q. Sheng, W. Cao, T. Yue and J. Zheng, *Biosens. Bioelectron.*, 2018, **113**, 142-147.
17 L. Wang, Y. Wang, J. I. Wong, T. Palacios, J. Kong and H. Y. Yang, *Small*, 2014, **10**, 1101-1105.
18 T. Wang, R. Zhu, J. Zhuo, Z. Zhu, Y. Shao and M. Li, *Anal. Chem.*, 2014, **86**, 12064-12069.
19 A. H. Loo, A. Bonanni, A. Ambrosi and M. Pumera, *Nanoscale*, 2014, **6**, 11971-11975.
20 C. F. Zhu, Z. Y. Zeng, H. Li, F. Li, C. H. Fan and H. Zhang, *J. Am. Chem. Soc.*, 2013, **135**, 5998-6001.
21 Y. Guo, Y. Shu, A. Li, B. Li, J. Pi, J. Cai, H.-H. Cai and Q. Gao, *J. Mater. Chem. B*, 2017, **5**, 5532-5538.
22 H. U. Kim, H. Y. Kim, A. Kulkarni, C. S. Ahn, Y. H. Jin, Y. Kim, K. N. Lee, M. H. Lee and T. Kim, *Sci. Rep.*, 2016, **6**, 34587.
23 L. L. Zhu, Y. Zhang, P. C. Xu, W. J. Wen, X. X. Li and J. Q. Xu, *Biosens. Bioelectron.*, 2016, **80**, 601-606.
24 S. H. Chen, R. Yuan, Y. Q. Chai and F. X. Hu, *Microchim. Acta*, 2013, **180**, 15-32.
25 W. Zhang, G. Fan, H. Yi, G. Jia, Z. Li, C. Yuan, Y. Bai and D. Fu, *Small*, 2018, **14**, 1703713.
26 D. R. Gough and T. G. Cotter, *Cell Death Dis.*, 2011, **2**, DOI: 10.1038/cddis.2011.1096.
27 M. H. Naveen, N. G. Gurudatt, H.-B. Noh and Y.-B. Shim, *Adv. Funct. Mater.*, 2016, **26**, 1590-1601.
28 B. Dou, J. Yang, R. Yuan and Y. Xiang, *Anal. Chem.*, 2018, **90**, 5945-5950.
29 R. J. Toh, C. C. Mayorga-Martinez, Z. Sofer and M. Pumera, *Adv. Funct. Mater.*, 2017, **27**, 1604923.
30 H. Song, Y. Ni and S. Kokot, *Biosens. Bioelectron.*, 2014, **56**, 137-143.
31 J. Zhou, Y. Zhao, J. Bao, D. Huo, H. Fa, X. Shen and C. Hou, *Electrochim. Acta*, 2017, **250**, 152-158.
32 W. Chen, S. Cai, Q.-Q. Ren, W. Wen and Y.-D. Zhao, *Analyst*, 2012, **137**, 49-58.
33 K. Kalantar-zadeh and J. Z. Ou, *ACS Sensors*, 2016, **1**, 5-16.
34 H. T. Wang, Z. Y. Lu, D. S. Kong, J. Sun, T. M. Hymel and Y. Cui, *ACS Nano*, 2014, **8**, 4940-4947.
35 I. S. Kwon, I. H. Kwak, H. G. Abbas, G. Jung, Y. Lee, J. Park, S. J. Yoo, J.-G. Kim and H. S. Kang, *Nanoscale*, 2018, **10**, 11349-11356.
36 J. Zhu, Z. Wang, H. Yu, N. Li, J. Zhang, J. Meng, M. Liao, J. Zhao, X. Lu, L. Du, R. Yang, D. Shi, Y. Jiang and G. Zhang, *J. Am. Chem. Soc.*, 2017, **139**, 10216-10219.
37 N. Liu, Y. Guo, X. Yang, H. Lin, L. Yang, Z. Shi, Z. Zhong, S. Wang, Y. Tang and Q. Gao, *ACS Appl. Mater. Interfaces*, 2015, **7**, 23741-23749.
38 X.-H. Zhang, N. Li, J. Wu, Y.-Z. Zheng and X. Tao, *Appl. Catal. B. Environ.*, 2018, **229**, 227-236.
39 Y. Shu, J. Chen, Q. Xu, Z. Wei, F. Liu, R. Lu, S. Xu and X. Hu, *J. Mater. Chem. B*, 2017, **5**, 1446-1453.
40 X. Y. Li and X. Z. Du, *Sensor. Actuat. B - Chem.*, 2017, **239**, 536-543.
41 N. Zhang and J. B. Zheng, *J. Mater. Sci.-Mater. Electron.*, 2017, **28**, 11209-11216.
42 S. Rostami, S. N. Azizi and S. Ghasemi, *J. Electroanal. Chem.*, 2017, **799**, 583-594.
43 C. Li, R. J. Wu, J. C. Zou, T. T. Zhang, S. F. Zhang, Z. Q. Zhang, X. Hu, Y. Q. Yan and X. M. Ling, *Biosens. Bioelectron.*, 2018, **116**, 81-88.
44 Y. Li, P. Zhang, Z. Ouyang, M. Zhang, Z. Lin, J. Li, Z. Su and G. Wei, *Adv. Funct. Mater.*, 2016, **26**, 2122-2134.
45 Y. Zhang, X. Bai, X. Wang, K.-K. Shiu, Y. Zhu and H. Jiang, *Anal. Chem.*, 2014, **86**, 9459-9465.
46 C. Zhang, H. Jiang, R. Ma, Y. Zhang and Q. Chen, *Ionics*, 2017, **23**, 1309-1317.
47 G. D. Nie, X. F. Lu, J. Y. Lei, L. Yang, X. J. Bian, Y. Tong and C. Wang, *Electrochim. Acta*, 2013, **99**, 145-151.
48 F. G. Xu, M. Deng, G. Y. Li, S. H. Chen and L. Wang, *Electrochim. Acta*, 2013, **88**, 59-65.
49 K. K. Rani, R. Devasenathipathy, S.-F. Wang and C. Yang, *Ionics*, 2017, **23**, 3219-3226.
50 B. Xue, K. Li, S. Gu, L. Zhang and J. Lu, *Sensor. Actuat. B - Chem.*, 2018, **262**, 828-836.
51 M. Victoria Bracamonte, M. Melchionna, A. Giuliani, L. Nasi,

View Article Online
DOI: 10.1039/C9NR00333A

C. Tavagnacco, M. Prato and P. Fornasiero, *Sensor. Actuat. B - Chem.*, 2017, **239**, 923-932.
52 J. Bai and X. Jiang, *Anal. Chem.*, 2013, **85**, 8095-8101.
53 S. Berbec, S. Zoladek, A. Jablonska and B. Palys, *Sensor. Actuat. B - Chem.*, 2018, **258**, 745-756.
54 A. Gupta, T. B. Rawal, C. J. Neal, S. Das, T. S. Rahman and S. Seal, *2D Mater.*, 2017, **4**, 025077.
55 X. Wang, Z. Chen, X. Zhao, T. Yao, W. Chen, R. You, C. Zhao, G. Wu, J. Wang, W. Huang, J. Yang, X. Hong, S. Wei, Y. Wu and Y. Li, *Angew. Chem. Int. Ed.*, 2018, **57**, 1944-1948.
56 M. Guler, V. Turkoglu, A. Bulut and M. Zahmakiran, *Electrochim. Acta*, 2018, **266**, 341-341.
57 T. C. Jorgenson, W. X. Zhong and T. D. Oberley, *Cancer Res.*, 2013, **73**, 6118-6123.
58 Y. Luo, H. Liu, Q. Rui and Y. Tian, *Anal. Chem.*, 2009, **81**, 3035-3041.
59 H. Dai, Y. Chen, X. Niu, C. Pan, H. Chen and X. Chen, *Biosens. Bioelectron.*, 2018, **118**, 36-43.
60 S. S. Chou, M. De, J. Kim, S. Byun, C. Dykstra, J. Yu, J. Huang and V. P. Dravid, *J. Am. Chem. Soc.*, 2013, **135**, 4584-4587.
61 D. Voiry, A. Goswami, R. Kappera, C. d. C. Castro e Silva, D. Kaplan, T. Fujita, M. Chen, T. Asefa and M. Chhowalla, *Nat. Chem.*, 2015, **7**, 45-49.

View Article Online
DOI: 10.1039/C9NR00333A

Graphic abstract

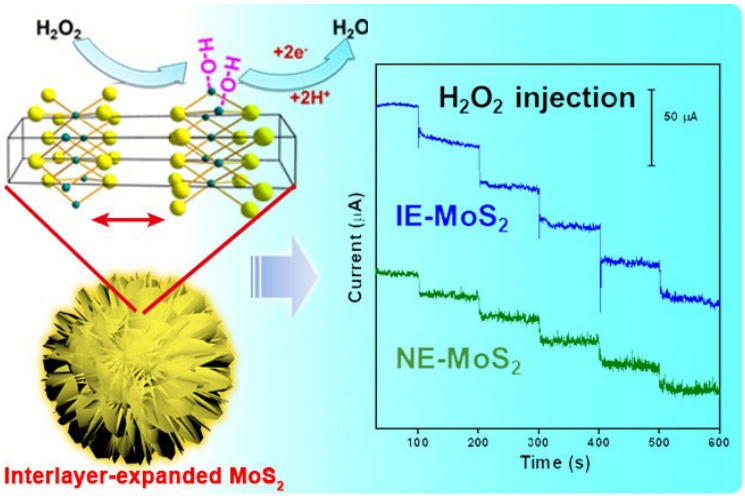

Interlayer-expanded MoS_2 is designed for efficient H_2O_2 sensing, thanks to its metallic electronic configurations and enhanced *OH binding.